



Ensemble design for seasonal climate predictions: Studying extreme Arctic sea ice lows with a rare event algorithm

Jerome Sauer¹, Francesco Ragone^{1,2}, François Massonnet¹, and Giuseppe Zappa³

¹Earth and Climate Research Center, Earth and Life Institute, Université catholique de Louvain, Louvain-la-Neuve, Belgium

²Royal Meteorological Institute of Belgium, Brussels, Belgium

³National Research Council of Italy, Institute of Atmospheric Sciences and Climate, Bologna, Italy

Correspondence: Jerome Sauer (jerome.sauer@uclouvain.be)

Abstract. Initialized ensemble simulations can help identify the physical drivers and assess the probabilities of weather and climate extremes based on a given initial state. However, the significant computational burden of complex climate models makes it challenging to quantitatively investigate extreme events with probabilities below a few percent. A possible solution to overcome this problem is to use rare event algorithms, i.e., computational techniques originally developed in statistical physics that increase the sampling efficiency of rare events in numerical simulations. Here, we apply a rare event algorithm to ensemble simulations with the intermediate complexity coupled climate model PlaSim-LSG to study extremes of pan-Arctic sea ice area reduction under pre-industrial greenhouse gas conditions. We construct seven pairs of control and rare event algorithm ensemble simulations each starting from seven different initial winter sea ice states. The rare event simulations produce sea ice lows with probabilities of at least two orders of magnitude smaller than feasible with the control ensembles, and drastically increase the number of extremes compared to direct sampling. We find that for a given probability level, the amplitude of negative late summer sea ice area anomalies strongly depends on the baseline winter sea ice thickness, but hardly on the baseline winter sea ice area. The experiments furthermore indicate a quasi-zero probability to internally generate a seasonally sea ice-free Arctic in this set-up. Finally, we investigate the physical processes in two trajectories leading to sea ice lows with conditional probabilities of less than 0.001%. In both cases, negative late summer pan-Arctic sea ice area anomalies are preceded by negative spring sea ice thickness anomalies. These are related to enhanced surface downward longwave radiative and sensible heat fluxes in an anomalously moist, cloudy and warm atmosphere. During summer, extreme sea ice area reduction is favoured by enhanced open-water-formation efficiency, anomalously strong downward solar radiation and the sea ice-albedo feedback. This work highlights that the most extreme summer sea ice conditions result from the combined effects of preconditioning and weather variability, emphasizing the need for thoughtful ensemble design when turning to real applications.

20 1 Introduction

Anthropogenic emissions of greenhouse gases have contributed to the loss of Arctic sea ice during the last 45 years (Notz and Marotzke, 2012; Stroeve and Notz, 2018; Gregory et al., 2002; Ding et al., 2017). Despite the steadily increasing rate of greenhouse gas concentrations (Meinshausen et al., 2017), the decline of the pan-Arctic sea ice area is non-linear, and internal climate variability and feedback mechanisms have been shown to modulate the downward trend of the sea ice (Ding et al.,



25 2017; Baxter et al., 2019; Ono et al., 2019; Francis and Wu, 2020; Tietsche et al., 2011). Accelerated decline of the late summer sea ice area occurred from the mid-2000s to 2012, resulting in record reductions of sea ice area compared to the trend line in 2007 and 2012.

30 The 2007 and 2012 drastic sea ice loss events have been attributed both to climate change via preconditioning through the ongoing winter sea ice thinning and to internal climate variability via particular weather and climate events during the melting season (Lindsay et al., 2009; Kauker et al., 2009; Zhang et al., 2008, 2013; Parkinson and Comiso, 2013; Kirchmeier-Young et al., 2017). The precise relative contributions of anthropogenically forced vs. internal climate variability to these events is, however, uncertain (Kirchmeier-Young et al., 2017; Ono et al., 2019). By applying an extreme event attribution analysis to ensemble simulations with the Second Generation Canadian Earth System Model (CanESM2), Kirchmeier-Young et al. (2017) concluded that a sea ice low with an amplitude as observed in 2012 (i.e. a 2012-like sea ice area anomaly relative to the observed 1981-2010 mean) would have been extremely unlikely to occur without global warming. Ono et al. (2019), instead, used a 200-year control simulation with a fixed year-2000 greenhouse gas forcing in the Model for Interdisciplinary Research on Climate (MIROC) version 5.2 and simulated a sea ice low larger in magnitude than the 2012 sea ice area anomaly relative to a linear trend line fitted to observed September sea ice area values between 1979 and 2006. In accordance with Kirchmeier-Young et al. (2017), however, the authors do not managed to simulate a sea ice area anomaly with a larger amplitude than the observed 2012 anomaly relative to the observed climatological mean between 1981 and 2010.

45 Various studies have analyzed the physical drivers of the 2007 and 2012 sea ice lows. In 2007, sea ice reduction was favoured by enhanced inflow of warm Pacific water through Bering Strait (Woodgate et al., 2010) and by anomalously persistent southerly winds in the Pacific sector associated with the Arctic Dipole Anomaly (ADA) pattern (Wang et al., 2009; Lindsay et al., 2009; Overland et al., 2012; Kauker et al., 2009). In 2012, a summer storm contributed to enhanced sea ice reduction by leading to increased bottom melt via anomalously strong vertical mixing in the oceanic boundary layer (Guemas et al., 2013; Zhang et al., 2013). Further possible triggers of anomalously low summer Arctic sea ice area include enhanced North Atlantic oceanic heat transport (Årthun et al., 2012), the positive and negative phases of the winter and summer Arctic Oscillation (AO) (e.g. Rigor et al. (2002); Ogi et al. (2016)), reduced cloudiness during summer (Schweiger et al., 2008), and increased surface downward longwave radiation related to enhanced poleward atmospheric moisture transport during spring (Kapsch et al., 2013, 2019).

55 Even though the physical drivers of individual extremes of Arctic sea ice reduction have been suggested, their quantitative statistical analysis is hampered by the small number of extreme events that can be sampled from observations and numerical simulations. Likewise, it is the small number of events in the lower tail of the distribution of sea ice area values that makes it challenging to quantify the probability of a 2012-like sea ice low event for a given background climate. The record of satellite-based sea ice observations includes only a few annual sea ice minima with orders of magnitude comparable to the ones in September 2007 and 2012 (Fetterer et al., 2017). Moreover, the large computational cost of complex climate models makes it unrealistic to run ensembles with a few thousands of trajectories and to quantitatively study extreme events with probabilities of less than 1%. One workaround is to estimate these very small probabilities with extreme value theory models (Coles, 2001).



65 However, even when applicable, these methods provide only a statistical extrapolation of the probabilities and do not provide
information on the dynamics. A better understanding of the precursors of extremes of summer Arctic sea ice reduction and
a more precise estimate of their probabilities are in turn crucial to improve seasonal predictions of these events and to assess
70 their risk of occurrence under different climate change scenarios.

In this work, we study extreme negative summer pan-Arctic sea ice area anomalies using initialized ensemble simulations
with the intermediate complexity coupled climate model PlaSim-LSG under pre-industrial greenhouse gas conditions. We
investigate the statistical properties of extreme summer sea ice lows as a function of different initial winter states and exam-
ine the physical drivers favouring extremes of sea ice area reduction within a single melting season. In order to improve the
75 sampling of extreme sea ice loss events, we use a rare event algorithm. Rare event algorithms are computational techniques
developed in statistical physics to improve the sampling efficiency of rare events in numerical simulations (e.g. Ragone et al.,
2018; Ragone and Bouchet, 2020, 2021; Sauer et al., 2024). Compared to conventional numerical simulations with the same
computational cost, rare event algorithms enable to increase the number of simulated extreme events by several orders of mag-
nitude while preserving the dynamical consistency of the model. In this way, these techniques allow to reduce the uncertainty
80 of probability and return time estimates and of conditional statistics on extreme events (e.g. composites) compared to con-
ventional simulation strategies, and to generate ultra-rare events that are very unlikely to be observed using direct sampling.
Rare event algorithms have been introduced in the 1950s (Kahn and Harris, 1951) and have been used since for a wide range
of applications (for an overview and the mathematical analysis see e.g. Del Moral (2004); Giardina et al. (2011); Grafke and
Vanden-Eijnden (2019)). Recently, some of these techniques have been applied in climate science and in fluid dynamics to
85 study heat waves (Ragone et al., 2018; Ragone and Bouchet, 2020, 2021), midlatitude precipitation (Wouters et al., 2023),
tropical storms (Plotkin et al., 2019; Webber et al., 2019), weakening and collapse of the Atlantic Meridional Overturning
Circulation (AMOC) (Cini et al., 2023), extreme Arctic sea ice lows related to unconditional probability distributions (Sauer
90 et al., 2024) and turbulence (Bouchet et al., 2018; Grafke et al., 2015; Lestang et al., 2020).

Here we use a genealogical selection algorithm (Ragone et al., 2018; Ragone and Bouchet, 2020, 2021; Sauer et al., 2024)
adapted from Del Moral and Garnier (2005); Giardina et al. (2011), that is efficient to study persistent, long lasting events. A
first application of this algorithm to study extreme Arctic sea ice lows in the intermediate complexity coupled climate model
PlaSim under pre-industrial greenhouse gas conditions is given in Sauer et al. (2024). In that study, ensemble simulations with
95 the rare event algorithm were initialized with independent initial conditions sampled from a stationary 3000-year control run
such that the statistics of extreme events is related to unconditional probability distributions. In such an approach, the rare event
algorithm seeks to oversample trajectories leading to low sea ice states in an absolute sense, i.e., independent from the extent to
which the sea ice lows are related to multi-annual fluctuations in the sea ice-ocean system (referred to as "preconditioning" in
Sauer et al. (2024)) or driven by the dynamics occurring on intra-seasonal time scales. Here, instead, we use a seasonal climate
100 prediction set-up where an ensemble simulation is initialized from a single initial condition to which a small perturbation is
added. We perform different ensemble simulations starting from different initial conditions sampled from the same control run
as in Sauer et al. (2024). The goal of these experiments is to disentangle the roles of the initial condition vs. seasonal scale

fluctuations in favouring the occurrence of extremely negative summer sea ice area anomalies. Since each individual ensemble simulation is initialized from a same, slightly perturbed initial condition, statistical and physical properties of low sea ice states inferred from that ensemble need to be interpreted in terms of conditional probabilities.

Owing to the rare event algorithm, we generate extremely low sea ice summers with conditional probabilities of less than 0.001%. Likewise, we investigate the impact of different initial conditions on the probabilities and amplitudes of extreme sea ice lows. Finally, we elaborate physical drivers in two trajectories leading to late summer sea ice lows with less than 0.001%. The paper is structured as follows. In section 2, we present the set-up of the model, the methodology of the rare event algorithm and the design of control and rare event algorithm ensemble simulations. In section 3, we show that the rare event algorithm improves the sampling efficiency of extreme sea ice lows conditional on starting from a certain initial condition compared to standard control ensemble simulations. We analyze the impact of the initial condition on the probabilities and amplitudes of the extremes. In section 4, we discuss physical processes and conditions in individual trajectories prior to extreme sea ice lows with probabilities with less than 0.001%. In section 5, we present our conclusions.

2 Materials and methods

2.1 Model and data

All simulations are performed with a coupled set-up of the intermediate complexity climate model Planet Simulator (PlaSim) version 17 (Fraedrich et al., 2005). This set-up includes a dynamic Large-Scale Geostrophic (LSG) ocean (Maier-Reimer et al., 1993; Drijfhout et al., 1996), a mixed-layer ocean and a thermodynamic sea ice model (PlaSim coupled to LSG is referred to as "PlaSim-LSG" in the following).

The atmosphere is run with a horizontal spectral resolution of T21 (triangular truncation at wavenumber 21 \sim 5.625° x 5.625° on a Gaussian grid), ten levels up to 40 hPa in the vertical and a computational time step of 45 minutes. The LSG is configured on a 2.5° x 5° staggered E-type grid (Arakawa and Lamb, 1977) in the horizontal, with 22 levels and a maximum ocean depth of 6000 m in the vertical and a computational time step of five days. The sea ice model is based on the zero-layer model of Semtner (1976). It computes the sea ice thickness and sea surface temperature evolution from the energy balances at the top and bottom of a sea ice-snow layer. The sea ice-snow layer is assumed to have a linear temperature gradient and to have no capacity to store heat. No sea ice drift is taken into account. The sea ice concentration is binary, i.e., a grid cell is fully sea ice covered or open water. The computational time step in the sea ice and mixed-layer ocean models is one day.

PlaSim-LSG is run with a fixed pre-industrial effective CO₂ volume mixing ratio of 280 ppmv. We choose a constant greenhouse gas forcing since we are interested in the statistics and dynamics of Arctic sea ice lows related to internal climate variability under a stationary climate. Solar radiation includes the seasonal cycle but not the diurnal cycle. Each model month is 30 days long.

We use data from a stationary 3000-year control run (Sauer et al., 2024) and from a set of control and rare event algorithm ensemble simulations (see section 2.2 for more details). We consider the statistics of the pan-Arctic sea ice area



$$A(t) = \sum_{\phi \geq \phi_{min}} \sum_{\lambda} SIC_{\phi,\lambda}(t) \cdot G_{\phi,\lambda}, \quad (1)$$

where $SIC_{\phi,\lambda}(t)$ is the sea ice concentration at time t in a grid cell centered at latitude ϕ and longitude λ , $G_{\phi,\lambda} =$
 145 $\int_{\phi - \frac{\Delta\phi}{2}}^{\phi + \frac{\Delta\phi}{2}} \int_{\lambda - \frac{\Delta\lambda}{2}}^{\lambda + \frac{\Delta\lambda}{2}} R^2 \cos(\phi') d\lambda' d\phi'$ is the grid cell area, R is the earth radius, $\Delta\phi$ and $\Delta\lambda$ are the angular distances between
 two grid points in the meridional and zonal direction. The summation in (1) includes all ocean grid boxes north of 40°N (i.e.
 $\phi_{min} \cdot \frac{180^\circ}{\pi} = 40^\circ$) with a binary land-sea mask (i.e. a grid cell is either completely ocean or land). The annual average, ampli-
 tude of the seasonal cycle and the timing of the annual minimum and maximum of the pan-Arctic sea ice area produced by the
 model are representative of the observed Arctic sea ice climatology between 1979 and 2015 (cf. Figure 1(a,c) of Sauer et al.
 150 (2024) and Figure S1 in the Supplementary Information of Sauer et al. (2024)). Differences in the representation of sea ice in
 PlaSim-LSG compared to observations include a delayed melting period, a positive sea ice concentration (SIC) bias from the
 Greenland to the Kara Sea and a negative SIC bias western of Greenland (cf. Figure 1(a,c) of Sauer et al. (2024) and Figure
 S1 in the Supplementary Information of Sauer et al. (2024)). All in all, however, the differences between the pan-Arctic sea
 ice area in PlaSim-LSG and in observational data are small compared to the range of sea ice area values available from the
 155 Coupled Model Intercomparison Project Phase 6 (CMIP6) models (Notz and SIMIP Community, 2020). The representation of
 sea ice in PlaSim-LSG is therefore sufficient for the purpose of this study.

We study extreme anomalies of February-September and August-September mean pan-Arctic sea ice area. We classify a sea
 160 ice area anomaly $I'(t)$ as extremely negative if $I'(t) \leq n\sigma_{ctrl}$, where σ_{ctrl} is the standard deviation of sea ice area in the control
 run or in a control ensemble (see section 2.2) and n is a real-valued number. In the following, we will vary n continuously to
 study an extensive range of extreme event amplitudes.

2.2 Rare event algorithm: Methodology and set-up

One key difficulty in the study of climate extremes is the lack of robust statistics as the large computational burden of complex
 165 climate models makes it unfeasible to run them long enough to sample a large amount of trajectories corresponding to the tail
 of the distribution of a target observable.

The rare event algorithm presented in recent studies (Giardina et al., 2011; Ragone et al., 2018; Ragone and Bouchet,
 170 2020, 2021; Sauer et al., 2024) is a genealogical selection algorithm applied on top of an ensemble simulation. It is designed to
 improve the sampling efficiency of trajectories populating the tail of the distribution of the time-average of a target observable
 $A(t)$. At constant intervals of a resampling time τ_r , we assign to each trajectory a weight. The weight is a function of the time-
 average of the observable during the past interval of duration τ_r for that trajectory. Before simulating the next time window
 of length τ_r , trajectories with small weights are removed from the ensemble and are substituted by slightly perturbed copies
 175 of trajectories with large weights. The algorithm includes a parameter k which controls the relative amplitude of the weights
 for given values of the target observable, where the case $k = 0$ would correspond to a regular ensemble simulation. If τ_r is not
 larger than the decorrelation time of the observable, then the selection will favour the survival of trajectories leading to extreme



anomalies of the time-average of a target observable such as the pan-Arctic sea ice area (positive for k positive and viceversa). We refer to Ragone et al. (2018); Ragone and Bouchet (2020, 2021); Sauer et al. (2024) for more details about the method and present here the main outcome.

We denote $X(t)$ the vector of all model variables at time t and T_a the total simulation time. We consider an ensemble of N trajectories $\{X_n(t)\}$ ($n = 1, 2, \dots, N$). Let $\mathbb{P}_0(\{X_n(t)\}_{0 \leq t \leq T_a})$ be the probability density of observing a given trajectory $X_n(t)$ from time 0 to time T_a in a direct numerical simulation with the model, and $\mathbb{P}_k(\{X_n(t)\}_{0 \leq t \leq T_a})$ be the probability density of the same trajectory in an ensemble simulation with the rare event algorithm with a given value of the parameter k . For a large ensemble size N the relation between the two is given by the importance sampling formula

$$\mathbb{P}_k(\{X_n(t)\}_{0 \leq t \leq T_a}) \underset{N \rightarrow \infty}{\sim} \frac{e^{k \int_0^{T_a} A(\{X_n(t)\}) dt}}{\mathbb{E}_0[e^{k \int_0^{T_a} A(\{X_n(t)\}) dt}] } \mathbb{P}_0(\{X_n(t)\}_{0 \leq t \leq T_a}), \quad (2)$$

where \mathbb{E}_0 is the expectation value with respect to \mathbb{P}_0 , $A\{X_n(t)\}$ the target observable and k a biasing parameter controlling the strength of the selection. Thanks to Equation (2), the expectation value according to \mathbb{P}_0 (the real statistics of the system) of a generic quantity $O(\{X_n(t)\}_{0 \leq t \leq T_a})$ can be estimated from data generated with the algorithm (which are instead distributed according to \mathbb{P}_k) as

$$\mathbb{E}_0[O(\{X_n(t)\}_{0 \leq t \leq T_a})] \underset{N \rightarrow \infty}{\sim} \frac{1}{N} \sum_{n=1}^N Z_k e^{-k \int_0^{T_a} A(\{X_n(t)\}) dt} \cdot O(\{X_n(t)\}_{0 \leq t \leq T_a}). \quad (3)$$

where Z_k is a constant factor computed by the algorithm (see Ragone et al. (2018); Ragone and Bouchet (2020)). Equation (3) shows that statistical quantities like composites, probabilities or return times with respect to the real model statistics can be estimated with data generated by the algorithm by weighting the contribution of each trajectory to sample averages by the inverse of the exponential factor which appears in the importance sampling formula. In Ragone et al. (2018), Ragone and Bouchet (2020, 2021) and Sauer et al. (2024), the trajectories appearing in (2) and (3) were generated from ensembles initialized with different initial conditions randomly selected from a control run to uniformly sample the attractor of the dynamics. In such an application, Equation (2) would refer to unconditional probabilities. In this work, however, the ensembles are initialized from single initial conditions and the probabilities and expectation values in (2) and (3) have to be interpreted as conditional on the selected initial state.

We use as target observable $A\{X_n(t)\}$ the pan-Arctic sea ice area and perform $M = 7$ ensemble simulations with the rare event algorithm initialised from seven different initial conditions. In order to have a baseline of the statistics, each experiment is accompanied by a control ensemble simulation (i.e. a simulation without applying the algorithm) with the same ensemble size, simulation length and initial condition as the one with the rare event algorithm. Each ensemble contains $N = 600$ trajectories and is run for a total simulation time $T_a = 240$ days from 01 February to 30 September.

The biasing parameter in the simulations with the rare event algorithm is $k = -0.075 \cdot 10^{-6} \text{ km}^{-2} \text{ day}^{-1}$. The precise value of k is chosen empirically. However, a reasonable order of magnitude of the parameter can be derived from the standard deviation



220 and decorrelation time of the sea ice area anomalies in the control ensembles using a scaling argument presented in Ragone
and Bouchet (2020) and in the Supporting Information of Ragone and Bouchet (2021). According to this scaling argument, the
selected k -value corresponds to a shift of the mean of the distribution of the February-September mean sea ice area to values
between approximately $0.15 \cdot 10^6 \text{ km}^2$ and $0.35 \cdot 10^6 \text{ km}^2$ below the means of the control ensembles. This corresponds to a
range of estimated probabilities between about 10% and 1% (see section 3.1).

225 The resampling time in the simulations with the rare event algorithm is $\tau_r = 5$ days. It is chosen to be not larger than the
persistence time scale of the large-scale atmospheric circulation (Baldwin et al., 2003) and to be only slightly larger than the
typical persistence of synoptic-scale atmospheric fluctuations (Hoven, 1957). The rare event simulations are therefore suitable
230 to improve the sampling efficiency of extremely low sea ice states both driven by oceanic processes and due to anomalies in
the atmospheric circulation that are in the order of or larger than the upper range of the synoptic time scale.

Within an individual ensemble, each trajectory starts from the same initial condition as done for ensemble weather and
235 seasonal climate predictions. In order to allow the trajectories to diverge from each other, we slightly perturb the surface
pressure field of each trajectory as described in the Supporting Information of Ragone et al. (2018). The seven different initial
conditions for the seven ensembles are sampled from the 3000-year control run according to different anomaly values of
the January-February mean pan-Arctic sea ice area, i.e. the observable itself, and of the January-February mean cumulative
area with sea ice thickness equal or larger than 1.93 m (SIT1.93, Figure 1 and table 1). The choice of SIT1.93 is motivated
240 by the studies of Chevallier and Salas-Mélia (2012) and Lindsay et al. (2008). According to those studies, the late winter-
early spring cumulative area with sea ice thickness larger than a critical threshold has a larger impact on the late summer sea
ice area than the winter-spring sea ice volume and area itself. Here we apply a composite analysis to the PlaSim-LSG
control run to identify a sea ice-related variable whose anomaly value during the timing of the ensemble initialization has a
potentially large connection with the probability of an extreme late summer sea ice low (Figure 1(a); note that the critical
245 thickness values of 0.2 m, 0.5 m, 0.66 m, 0.9 m, 1.5 m, 1.93 m, 2.5 m, 4 m, 4.2 m, 6 m are selected from Chevallier and
Salas-Mélia (2012) and Lindsay et al. (2008)). Compared to the various variables shown in Figure 1(a), extremely negative
February-September and August-September mean sea ice area anomalies are most strongly related to the January-February
sea ice volume and cumulative area with sea ice thickness equal or larger than a critical thickness between 1.8 m and 2.1 m
respectively. We choose SIT1.93 following the critical threshold used in Lindsay et al. (2008). We emphasize, however, that
250 the labeling ("SIT1.93–", "SIT1.93=", "SIT1.93+") of the selected initial conditions would be the same as in this study if the
labeling were chosen according to the anomaly values of the cumulative area with sea ice thickness equal or larger than the
remaining thresholds between 1.80 m and 2.10 m. In PlaSim-LSG, the correlations between SIT1.93 and the cumulative area
with sea ice thickness equal or larger than the remaining thresholds between 1.8 m and 2.1 m are between 0.96 and 0.99, and
the precise choice of a threshold between 1.8 m and 2.1 m does not affect the interpretation of the results.

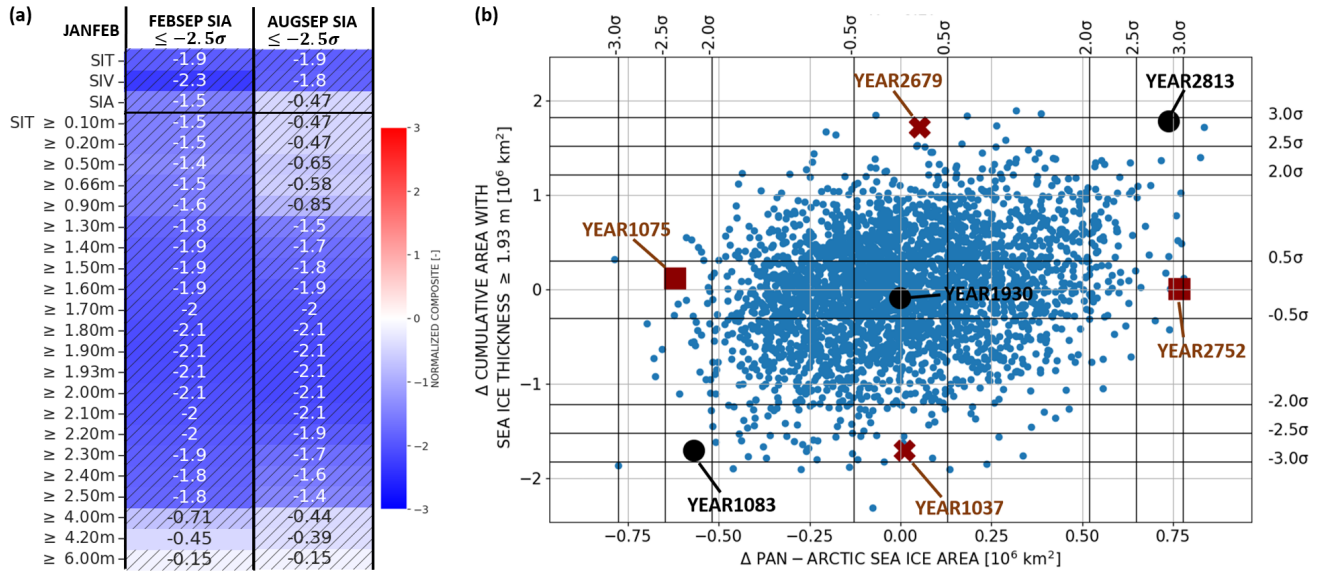


Figure 1. PlaSim-LSG 3000-year control run (Sauer et al. (2024)): (a) Normalized mean anomalies of January-February mean quantities conditional on extreme negative (left) February-September (FEBSEP) and (right) August-September (AUGSEP) mean pan-Arctic sea ice area anomalies equal or smaller than -2.5σ . "SIV", "SIA" and "SIT" are the pan-Arctic sea ice volume, sea ice area and mean sea ice thickness. "SIT \leq threshold" are anomalies in the cumulative area with sea ice thickness equal or larger than a critical threshold. Hatching denotes statistical significance at the 5% level assessed from a two-sided t-test applied to five composite estimates after subdividing the 3000-year control run into five 600-member ensembles. (b) Scatter plot of January-February mean anomalies of SIT1.93 vs. pan-Arctic sea ice area including the years from the selected initial conditions.

Table 1. 600-member control and rare event algorithm ensemble simulations running between 01 February and 30 September. Labeling of the experiments according to the different initial conditions with (middle column) the full label and (right column) short labels used in the text.

Control run year	Full label	Short label
1083	SIA-LOW SIT1.93-LOW	SIA – SIT1.93–
1037	SIA-NEUTRAL SIT1.93-LOW	SIA= SIT1.93–
1075	SIA-LOW SIT1.93-NEUTRAL	SIA – SIT1.93=
1930	SIA-NEUTRAL SIT1.93-NEUTRAL	SIA= SIT1.93=
2752	SIA-LARGE SIT1.93-NEUTRAL	SIA+ SIT1.93=
2679	SIA-NEUTRAL SIT1.93-LARGE	SIA= SIT1.93+
2813	SIA-LARGE SIT1.93-LARGE	SIA+ SIT1.93+



255 3 Results

3.1 Importance sampling of extreme sea ice lows and estimation of their probabilities

We exploit initialized ensemble simulations to investigate the statistical properties of extreme negative February-September and August-September mean pan-Arctic sea ice area anomalies as a function of seven different initial winter sea ice states (cf. section 2.2). The goal of using the rare event algorithm is to obtain a better statistics of extremely low sea ice area values than
260 available from standard control ensemble simulations. Compared to the latter, the algorithm likewise allows to better infer the order of magnitude of a lower bound of sea ice area values that can be generated internally via atmosphere-ocean dynamics.

We show the time evolution of pan-Arctic sea ice area anomalies relative to the control ensemble mean and the distributions
265 of summer sea ice area for the ensemble simulations starting from a neutral initial winter sea ice state (Figure 2(a,c,e); control run model year 1930 and labeled as "SIA= SIT1.93="; see section 2.2 for more details) and from an initial winter state characterized by neutral sea ice area and extremely low cumulative area with sea ice thickness equal or larger than 1.93 m (SIT1.93; Figure 2(b,d,f); control run model year 1037 and labeled as "SIA= SIT1.93–"). Among all seven experiments, the "SIA= SIT1.93=" rare event simulation delivers the trajectory with the most extreme negative August-September mean sea
270 ice area anomaly relative to the corresponding control ensemble mean (i.e. relative to the climatological mean value defined for the neutral sea ice initial condition), and the "SIA= SIT1.93–" experiment produces the trajectory leading to the lowest August-September mean sea ice area value in an absolute sense (cf. Figure 2 and Supplement Figures S2-S4).

275 Both in the "SIA= SIT1.93=" and "SIA= SIT1.93–" experiments, the differences between the sea ice area in the rare event algorithm and the control ensembles are small compared to the control intra-ensemble standard deviation until June (Figure 2(a,b)). From the end of June onwards, trajectories generated with the rare event algorithm show a systematic shift towards lower sea ice area values compared to the control ensembles, reaching an ensemble mean shift of about $-1.2 \cdot 10^6 \text{ km}^2$ in each case.

280 The biasing towards negative sea ice area anomalies with the rare event algorithm compared to the control ensemble reflects the importance sampling of extreme negative sea ice area anomaly values on average over the entire simulation period between February and September (Figure 2(c-d)) [cf. Sauer et al. (2024); Ragone and Bouchet (2021)]. The distributions of
285 February-September mean sea ice area obtained with the rare event algorithm fluctuate around a mean value in the lower tail of the control distribution, and their minimum sea ice area values are smaller than the minima obtained with the corresponding control ensembles (minimum February-September mean sea ice area values of $9.69 \cdot 10^6 \text{ km}^2$ and $9.26 \cdot 10^6 \text{ km}^2$ in the "SIA= SIT1.93=" and "SIA= SIT1.93–" rare event simulations vs. $9.88 \cdot 10^6 \text{ km}^2$ and $9.34 \cdot 10^6$ in the corresponding control ensemble simulations). As the February-September mean sea ice area is strongly related to the August-September one (the minimum-
290 maximum range of the correlation between both quantities across the members in all seven control ensembles is [0.89 0.94]), the algorithm likewise improves the sampling efficiency of extremely low August-September mean sea ice area exceeding the lower range of sea ice area values obtained with the control ensembles (Figure 2(e-f)); minimum August-September mean sea ice area values of $2.82 \cdot 10^6 \text{ km}^2$ and $2.07 \cdot 10^6 \text{ km}^2$ in the "SIA= SIT1.93=" and "SIA= SIT1.93–" rare event simulations vs.

3.54 · 10⁶ km² and 2.37 · 10⁶ in the control ensemble simulations).

295 It is noticeable that the sea ice area obtained with the control and rare event ensemble simulations depends on the chosen
initial condition (i.e. its location relative to the distribution of the 3000-year control run varies among the different experiments;
cf. Figure 2(c-f) and Supplement Figure S2-S4). In order to quantify the impact of the initial condition on extreme summer
300 sea ice lows, we compare the probability of extreme negative February-September and August-September mean sea ice area
anomalies between the seven experiments (Figure 3). We compute these probabilities as

$$P(a) = \frac{1}{N} \sum_{n=1}^N \mathbb{1}_a(I_n) \text{ with } \mathbb{1}_a(I_n) = \begin{cases} 1, & I_n \leq a \\ 0, & I_n > a \end{cases}, \quad (4)$$

where I_n is the February-September or August-September time-averaged pan-Arctic sea ice area in trajectory n , a is the
amplitude of the sea ice area anomaly, N the number of trajectories and $\mathbb{1}_a(I_n)$ is the indicator function. As Equation (4) rep-
305 resent the probability as an expectation value of the indicator function, probabilities from the simulations with the rare event
algorithm can be computed by applying the estimator in Equation (3) to this quantity (see Lestang et al. (2018), Ragone et al.
(2018); Ragone and Bouchet (2020) and Sauer et al. (2024)).

310 In Figure 3, the solid and dashed lines show the probabilities estimated with the control and rare event algorithm ensemble
simulations respectively. The control and rare event algorithm estimates are consistent with each other where they overlap.
Compared to the control ensembles, the major advantage of the algorithm is the access to much rarer events with the former
than the latter, reaching probability values of 10⁻⁵ (0.001%) for a computational cost of order 10²-10³. The plateaus at prob-
ability values smaller than 10⁻⁴ are likely due to undersampling as discussed in Lestang et al. (2018) and in the Supporting
315 Information of Ragone et al. (2018).

For a fixed probability level, the amplitudes of February-September and August-September mean sea ice area span a range
of about five and four and a half standard deviations among the different initial conditions. This confirms a strong impact of the
320 initial condition on the amplitudes and probabilities of extreme negative summer sea ice area anomalies evaluated relative to the
3000-year control run baseline climatology (Figure 3). Regarding the February-September seasonal average, both a low state in
the winter SIT1.93 and in the winter sea ice area contribute to the preconditioning of an extreme (Figure 3(a)). Consequently,
the most extremely negative seasonally averaged sea ice area anomalies occur following years with both a low winter state in
the sea ice area and in SIT1.93 (Figure 3(a)). The contribution of low winter sea ice area and low SIT1.93 to these anomalies,
325 however, is not fully additive (Figure 3(a)). For a fixed probability level, the sum of the February-September mean sea ice area
anomalies relative to the control run mean over the "SIA= SIT1.93=" and "SIA- SIT1.93=" experiments exceeds in magni-
tude the sea ice area anomalies obtained with the "SIA- SIT1.93=" experiment. We hypothesize that the preconditioning of
low states of the seasonally mean sea ice area through low winter sea ice area and SIT1.93 is efficient only for a restricted
geographic region where the climatological mean sea ice thickness is small enough to be able to form open water within one
330 season. In parts of that region, the contribution of low winter sea ice area and SIT1.93 to an anomalously large area of open
water during summer is likely to overlap spatially (i.e. open water conditions prevail in certain grid boxes independent from



whether both winter sea ice area and SIT1.93 are in a low state or only one of them). Regarding the August-September mean, the contribution of a low winter sea ice area to an extreme is small compared to the contribution of a low winter state in SIT1.93 (Figure 3(b)). Thus, similar amplitudes of extremely low August-September sea ice area occur for all three experiments with a
335 neutral SIT1.93, independent from the state of the winter sea ice area. Likewise, the most extremely low August-September sea ice area occurs in the experiment starting from an initial condition with a low SIT1.93 and a neutral winter sea ice area. A low winter sea ice area is therefore not required to produce the most extremely negative August-September sea ice area anomalies.

340 Despite the important role of preconditioning in favouring extremely low sea ice states, preconditioning represents only a necessary and not a sufficient condition for extremes with the largest amplitudes available in this study (Figure 3 and table 2). The most extreme sea ice lows occur as a consequence both of winter sea ice-ocean preconditioning and anomalous intra-seasonal processes (e.g. weather patterns; see section 4) that enhance sea ice reduction within one single melting season. The relative contribution of preconditioning to extreme sea ice lows vs. anomalous dynamics on an intra-seasonal time scale is
345 larger for February-September than August-September mean sea ice area (Figure 3 and table 2). Thus, the February-September time-averaged control ensemble mean sea ice area anomaly for the "SIA– "SIT1.93–" initial condition explains about 50% of the most extremely negative February-September mean sea ice area anomaly occurring in the "SIA– "SIT1.93–" rare event algorithm simulation. In contrast, the August-September time-averaged control ensemble mean sea ice area anomaly for the experiments starting from "SIT1.93–" are in the order of 30%-35% of the most extremely negative August-September mean
350 sea ice area anomalies appearing in the ensemble simulations with the rare event algorithm (Figure 3 and table 2).

Finally, it is striking that despite the fact that the algorithm favours the sampling of extremely low sea ice area values, no seasonally sea ice-free Arctic occurs in the simulations in the present study. Even in the experiment with a "SIT1.93-" initial
355 condition, i.e. an initial state being particularly favourable for low late summer sea ice states according to Figure 1, the most extremely low August-September mean sea ice area does not show values below the order of $2 \cdot 10^6$ km². Consequently, a seasonally sea ice-free Arctic generated by internal climate variability under the pre-industrial greenhouse gas forcing used in
360 this study has a quasi-zero probability.

The results obtained in Figure 3 are consistent with the memory properties of the sea ice in the Arctic. Typically, late summer sea ice area anomalies are poorly connected to the late winter sea ice area (Blanchard-Wrigglesworth et al., 2011; Chevallier and Salas-Mélia, 2012), explaining the non-existing contribution of winter sea ice area anomalies to extreme late summer sea ice area lows. Quantities related to the sea ice thickness, as shown in Chevallier and Salas-Mélia (2012), instead, act as a
365 preconditioning for extreme reduction of sea ice area via its impact on the open-water formation efficiency during summer. The dependency of extreme negative seasonally-averaged sea ice area anomalies on the winter sea ice area is explainable by the persistence of negative sea ice area anomalies from late winter to spring (Blanchard-Wrigglesworth et al., 2011).

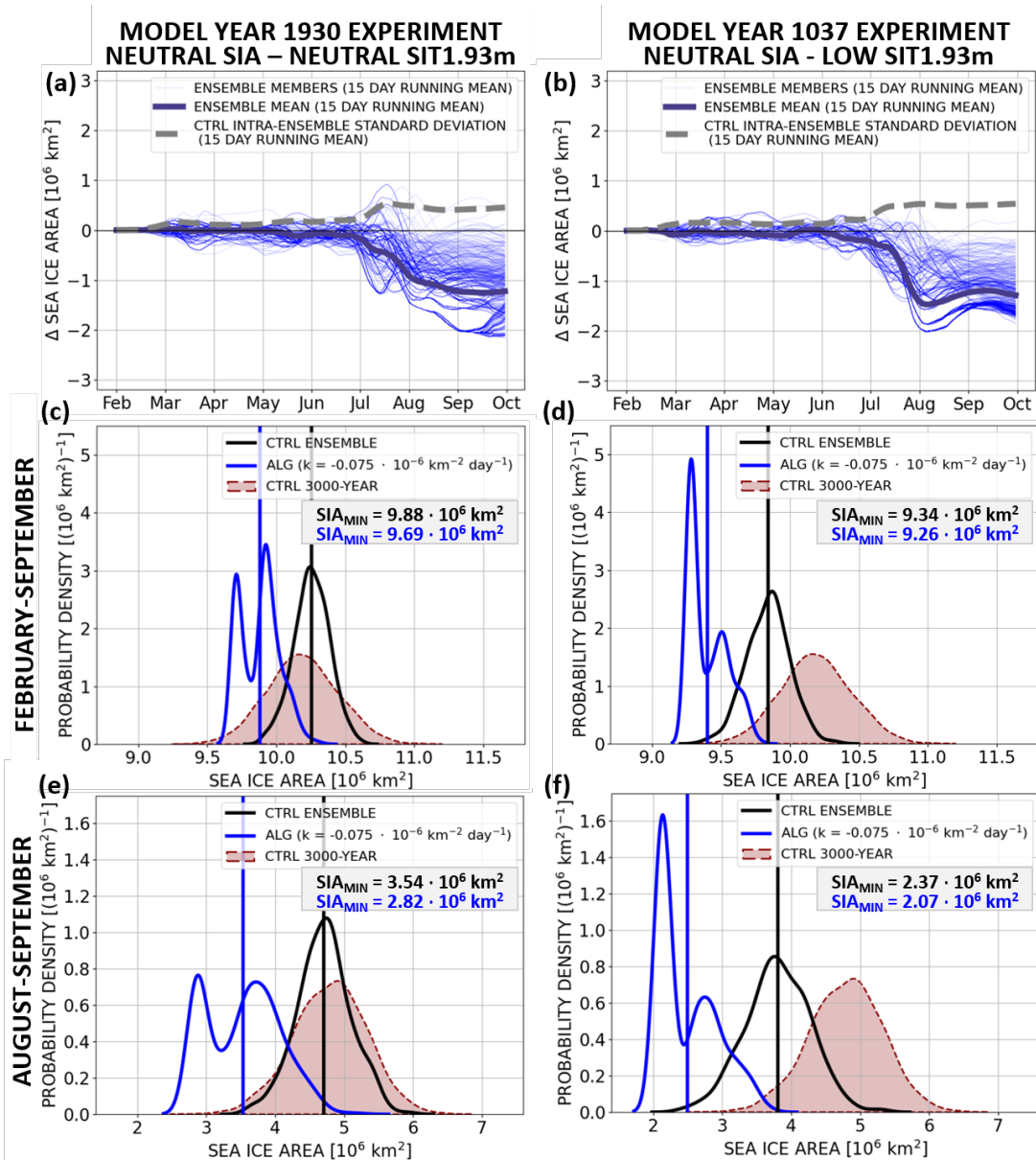


Figure 2. Ensemble simulations initialized on 01 February (a,c,e) 1930 and (b,d,f) 1037 of the control run. (a-b) Rare event simulations: Trajectories (thin blue lines) and ensemble mean (thick blue line) of daily pan-Arctic sea ice area anomalies relative to the daily climatology of the corresponding control ensembles. The gray dashed lines show the intra-ensemble standard deviations in the control ensembles. All lines are presented as 15-day running means. (c-f) Probability distribution functions of (c-d) February-September and (e-f) August-September mean pan-Arctic sea ice area for (blue) the rare event simulation, (black) the control ensembles and (red) the full 3000-year control run. The vertical lines show the mean of the distributions. The black and blue values indicate the smallest February-September and August-September mean sea ice area value sampled with the control and rare event ensemble simulations respectively.

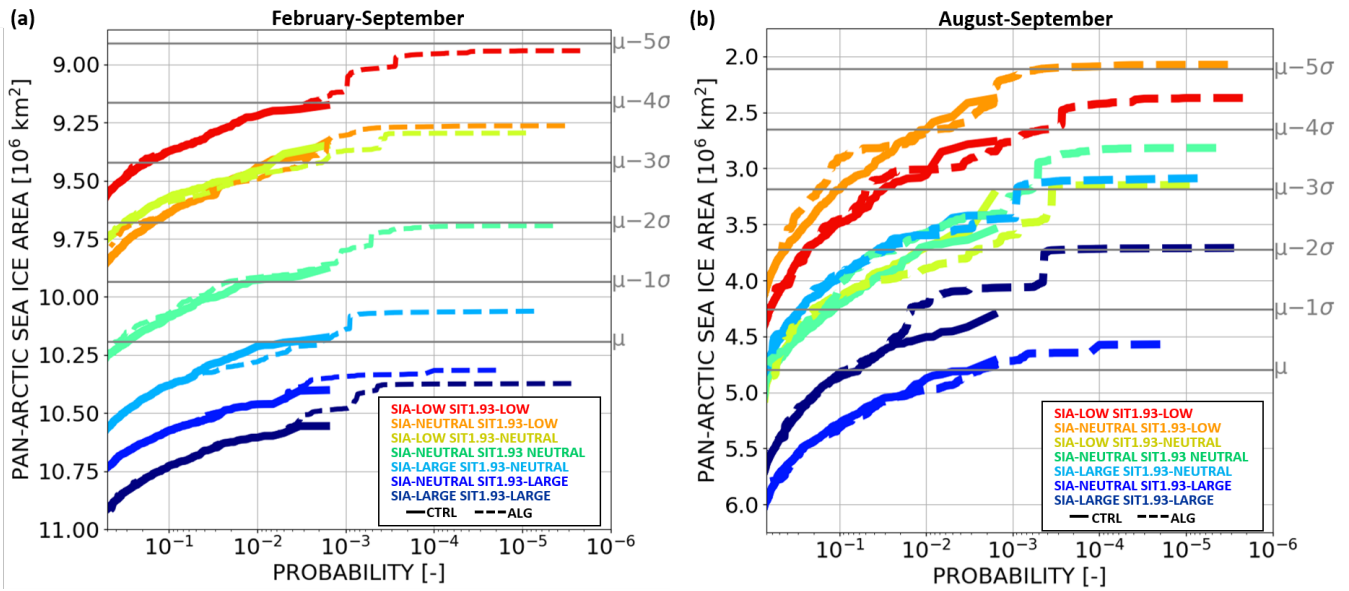


Figure 3. Probabilities (x -axes) of (a) February-September and (b) August-September mean sea ice area equal or smaller than a given threshold (y -axes) as a function of seven different initial conditions for (solid lines) the control ensembles and (dashed lines) for the algorithm. Note that the y -axes are displayed in reverse order. In the legend, “SIA” and “SIT1.93” indicate the state of the January-February mean anomaly of the pan-Arctic sea ice area and the cumulative area with sea ice thickness equal or larger than 1.93 m respectively. The grey labels on the right of each panel show how many standard deviations a sea ice area value is below the mean of the 3000-year control run.

Table 2. February-September (FEBSEP) and August-September (AUGSEP) mean sea ice area anomalies relative to the mean μ of the 3000-year control run for the trajectory with the most extremely negative sea ice area anomaly obtained with the rare event algorithm ($SIA_{\text{MIN}} - \mu$; i.e. preconditioning + anomalous weather) and for the control ensemble means ($\mu_{\text{ENS}} - \mu$; i.e. the impact of preconditioning on the mean of the control ensemble). “ $n\sigma$ ” denotes the unit of multiple control run standard deviations with $n \in \mathbb{R}$.

	FEBSEP		AUGSEP	
Initial condition	$(SIA_{\text{MIN}} - \mu)$ [$n\sigma$]	$(\mu_{\text{ENS}} - \mu)$ [$n\sigma$]	$(SIA_{\text{MIN}} - \mu)$ [$n\sigma$]	$(\mu_{\text{ENS}} - \mu)$ [$n\sigma$]
SIA– SIT1.93–	–4.87	–2.46	–4.52	–1.32
SIA= SIT1.93–	–3.61	–1.36	–5.07	–1.84
SIA– SIT1.93=	–3.49	–1.72	–3.07	–0.19
SIA= SIT1.93=	–1.94	+0.25	–3.68	–0.16
SIA+ SIT1.93=	–0.51	+1.48	–3.18	–0.48
SIA= SIT1.93+	+0.48	+2.14	–0.42	+1.81
SIA+ SIT1.93+	+0.71	+2.81	–2.02	+1.19



370 4 Physical processes and conditions prior to sea ice lows with probabilities of less than 0.001%

In this section we study the physical processes and conditions favouring extremely low late summer sea ice area. In contrast to the work in Sauer et al. (2024), the development of low sea ice states relative to the initial condition-specific control ensemble mean are entirely attributable to intra-seasonal drivers as all trajectories within an ensemble start from the same initial condition. Using the "SIA= SIT1.93=" and "SIA= SIT1.93—" experiments, we discuss the trajectory leading to the lowest August-September mean pan-Arctic sea ice area value available from the two experiments (Figures 4-7). The lowest August-September mean sea ice area values in the "SIA= SIT1.93=" and "SIA= SIT1.93—" ensembles are $2.82 \cdot 10^6 \text{ km}^2$ and $2.07 \cdot 10^6 \text{ km}^2$ and thus about 40% and 45% smaller than the control ensemble mean values of $4.71 \cdot 10^6 \text{ km}^2$ and $3.81 \cdot 10^6 \text{ km}^2$. These sea ice area anomalies are therefore larger in magnitude than the deviation of the observed 2012 mean August-September mean sea ice area from a trend line fitted to the period 1979-2006 (about -32%; $3.09 \cdot 10^6 \text{ km}^2$ compared to $4.53 \cdot 10^6 \text{ km}^2$; see Figure S1 in the Supplementary Information). The estimated probabilities to generate a sea ice area equal or smaller in absolute value than the one of the trajectories of the two ensemble simulations are $P=0.45 \cdot 10^{-5}$ ("SIA= SIT1.93=") and $P=0.33 \cdot 10^{-5}$ ("SIA= SIT1.93—" (see Figure 3).

385 4.1 Seasonal evolution of the state of the sea ice

The most dominant negative sea ice area anomalies in both trajectories start to develop in June-July and reach their peak amplitudes in August-September (Figure 4(a,d)). Negative August-September mean sea ice area anomalies are characterized by enhanced open water area in the Barents and Kara Seas, the eastern central Arctic Ocean and northern of the Canadian Archipelago (Figure 4(b,e)). From late winter to late spring, sea ice area anomalies are close to zero in the "SIA= SIT1.93=" experiment and slightly negative with a magnitude in the order of the intra-ensemble standard deviation in the "SIA= SIT1.93—" experiment. The fact that winter-spring sea ice area anomalies are small compared to the late summer supports the conclusion from Figure 3 that winter-spring sea ice area anomalies do not play an important role for the formation of late summer sea ice lows.

It is noticeable that late summer negative sea ice area anomalies are preceded by negative pan-Arctic sea ice volume anomalies starting to develop in spring (Figure 4(a,d)). These are related to the development of negative sea ice thickness anomalies before an anomalous reduction of the pan-Arctic sea ice area. These negative sea ice thickness anomalies develop predominantly on the Eurasian side of the Arctic and northern of the Canadian Archipelago (Figure 4(c,f)). They act as a preconditioning for enhanced open water formation in late summer as described in Chevallier and Salas-Mélia (2012).

4.2 Seasonal evolution of the state of the atmosphere

We are interested in the processes favouring the development of negative sea ice thickness and ensuing negative sea ice area anomalies. Firstly, we analyze the seasonal evolution of two metre temperature (T2M) and 500 hPa geopotential height (Z500) anomalies to establish a link between sea ice lows and the thermodynamic and dynamic states of the atmosphere (Figure 5). The evolution of the atmospheric state differs between the "SIA= SIT1.93=" and "SIA= SIT1.93—" trajectories. In the "SIA=

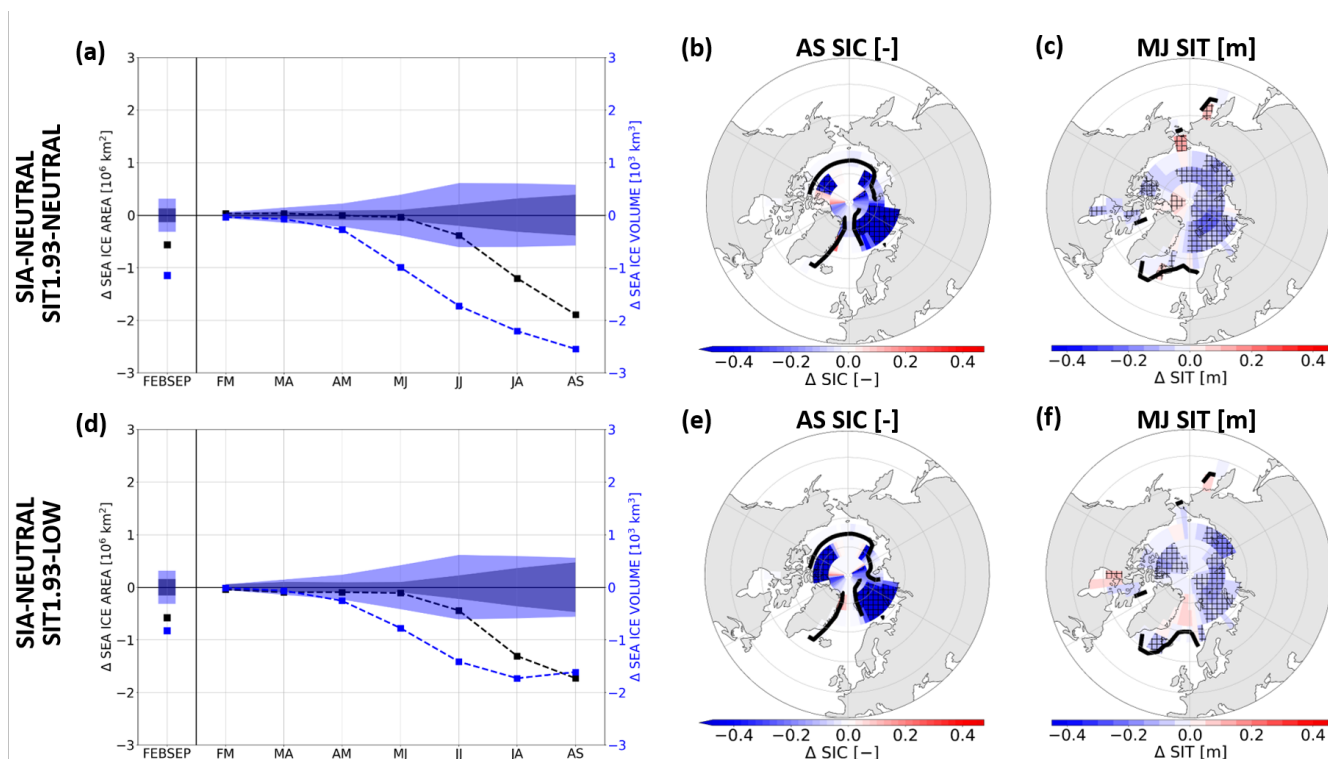


Figure 4. Trajectory with the lowest February-September and August-September mean pan-Arctic sea ice area in the rare event algorithm ensemble simulation starting from a winter initial condition characterized by (a-c) neutral sea ice area and neutral SIT1.93 (control run year 1930) and (d-f) neutral sea ice area and low SIT1.93 (control run year 1037). (a,d) Pan-Arctic sea ice (black) area [10^6 km^2] and (blue) volume [10^3 km^3] anomalies. Shading shows the intra-ensemble standard deviation of the corresponding control ensembles. (b,e) August-September mean sea ice concentration and (c,f) May-June mean sea ice thickness anomalies. Hatching indicates anomalies larger in magnitude than the intra-ensemble standard deviation. (a-f) All anomalies are computed with respect to the climatology of the corresponding control ensembles.

SIT1.93=" trajectory, the Arctic region is in an anomalously warm state from late winter to late spring. Positive T2M anomalies occur over the central Arctic Ocean in February-March and show a wavenumber 3-like positive T2M pattern in spring associated with a baroclinic signal in the 500 hPa geopotential height anomaly field (Figure 5(b,c,g,h)). In May-June, anomalously warm conditions prevail over the eastern Arctic and north of the Canadian Archipelago, and thus spatially coincide with the region of negative sea ice thickness anomalies (cf. Figures 5(c) and Figure 4(c)). In June-July, the magnitude of T2M anomalies declines as two metre temperatures are constrained by the climatological sea ice melting to be close to the freezing point. The reemergence of anomalously warm conditions in July-August may both be a driver of sea ice reduction and a consequence of reduced sea ice conditions. In contrast to the "SIA= SIT1.93=" experiment, the "SIA= SIT1.93—" trajectory shows an anomalously cold near-surface atmosphere in February-March followed by a strong warming with a barotropic positive geopotential height anomaly response during spring (Figure 5(k,l,m,p,q,r)). Positive 500 hPa geopotential height anomalies persist until summer, while T2M are constrained to be close to the freezing point in June-July before reemerging in August-September as



for the "SIA= SIT1.93=" trajectory (cf. Figures 5(n,o,s,t) and 5(d)).

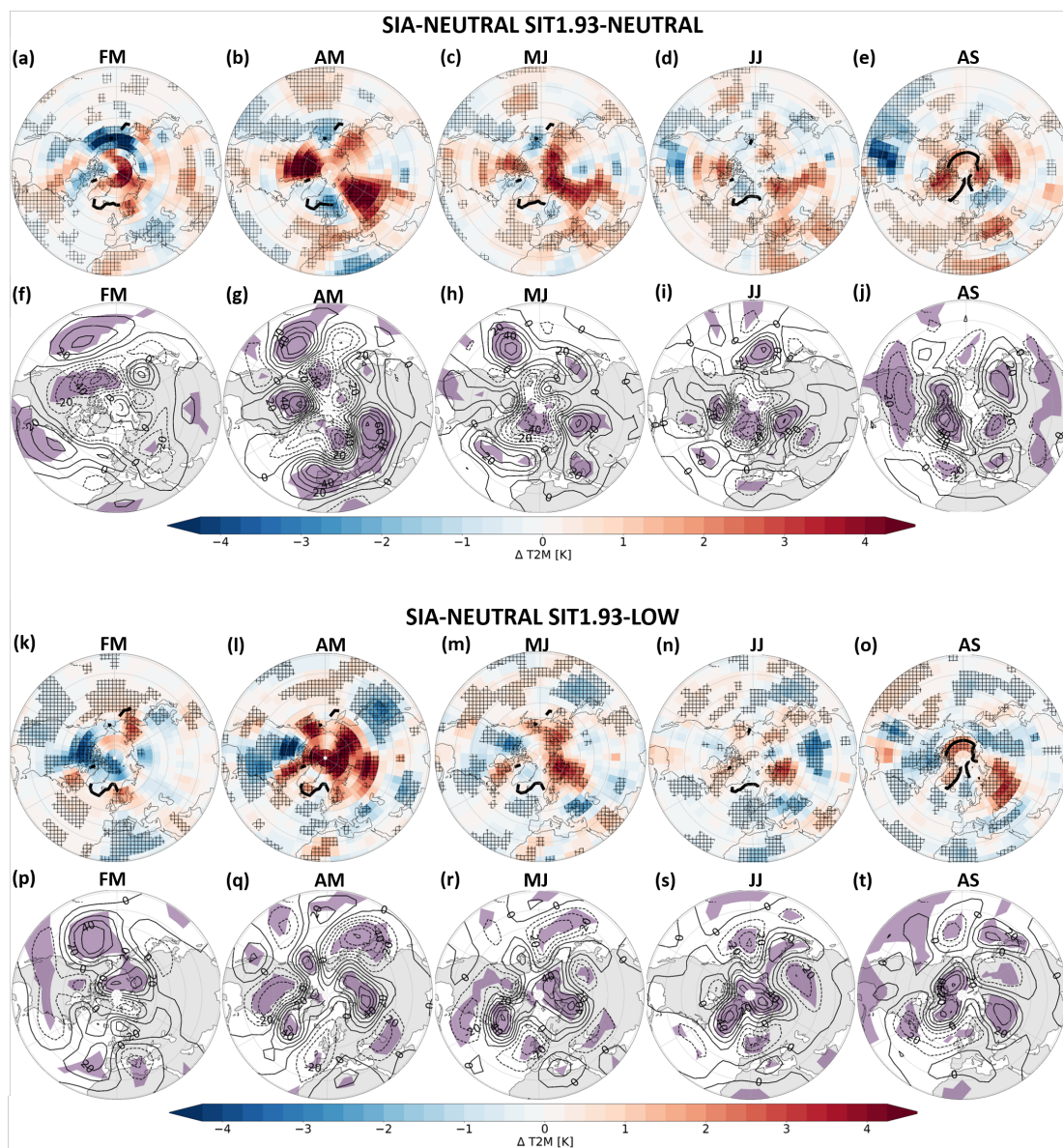


Figure 5. Trajectory with the lowest February-September and August-September mean pan-Arctic sea ice area in the rare event algorithm ensemble simulation starting from a winter initial condition characterized by (a-j) neutral sea ice area and neutral SIT1.93 (control run year 1930) and (k-t) neutral sea ice area and low SIT1.93 (control run year 1037). (a-e) and (k-o) February-March (FM), April-May (AM), May-June (MJ), June-July (JJ) and August-September (AS) mean T2M anomalies [K] and (f,j) and (p-t) FM, AM, MJ, JJ, AS mean Z500 anomalies [gpm]. Contour interval for Z500 is 10 gpm. Hatching indicates anomalies larger in magnitude than the intra-ensemble standard deviation. All anomalies are computed with respect to the climatology of the corresponding control ensembles. The black contour line in (a-e) and (k-o) shows the climatological sea ice edge defined as the 15% sea ice concentration contour line.



420 4.3 Surface energy budget analysis

We perform a surface energy budget analysis to understand how the anomalous reduction of sea ice is physically related to anomalous atmospheric conditions (Figures 6-7). We define the surface energy budget for an infinitesimally thin interface without heat storage located between the atmosphere and the snow-sea ice-ocean system (cf. Serreze and Barry (2014)). The different terms of the budget are then given by

$$425 \quad R_{SW}(1 - \alpha) + R_{LW} + S + L = -\epsilon\sigma T_s^4 + Q + M, \quad (5)$$

where R_{SW} and R_{LW} are the downward shortwave and downward longwave radiative fluxes, respectively; α is the surface albedo, S and L are the sensible and latent heat fluxes, ϵ is the surface emissivity, $\sigma = 5.67 \cdot 10^{-8} \text{ W m}^{-2} \text{ K}^{-4}$ is the Stefan–Boltzmann constant and T_s is the surface temperature. Q summarizes conductive and turbulent energy fluxes between the surface and the snow-sea ice-ocean system. M is the energy flux associated with melting and freezing at the surface. Energy
430 fluxes related to bottom sea ice growth, to temperature changes in the snow-sea ice-ocean system and the vertical energy flux from the ocean into the sea ice are implicitly included in Q . In Figure 6, we complement the analysis of the atmosphere-surface energy fluxes by the analysis of the vertical oceanic heat flux. If not stated otherwise, we define upward (downward) energy
435 fluxes and associated flux anomalies to be positive (negative).

Both in the "SIA= SIT1.93=" and "SIA= SIT1.93–" trajectories, strongly negative net surface-atmosphere energy flux anomalies occur over the Arctic Ocean from April-May to August-September, indicating an anomalous energy accumulation within the snow-sea ice-ocean system (Figure 6(a,b)). Anomalies in the vertical oceanic heat flux are much smaller than the atmospheric ones, but still systematically positive in summer in both trajectories (Figure 6(a,b)). Slightly positive vertical oceanic
440 heat flux anomalies in late winter in "SIA= SIT1.93–" together with enhanced heat loss from the surface to the atmosphere indicate a small oceanic forcing on the reduction of sea ice, contributing to the small negative late winter-spring sea ice area anomalies shown in Figure 4(d).

The contribution of different flux components to the negative net atmosphere-surface energy flux anomalies varies among the season and between the two trajectories. In the "SIA= SIT1.93=" trajectory, two distinct phases exist. In spring, enhanced net energy accumulation in the snow-sea ice-ocean system is predominantly explained by negative net longwave radiative flux anomalies and enhanced downward sensible heat fluxes (Figure 6(c,e)). During summer, the anomalies in the atmosphere-surface energy transfer are dominated by the shortwave fluxes. Qualitatively, the two phases are apparent also in the "SIA= SIT1.93–" trajectory (Figure 6(d,f)). Compared to the "SIA= SIT1.93=" trajectory, however, the enhanced longwave radiative
450 forcing on the sea ice has a smaller duration exceeding the intra-ensemble standard deviation exclusively in April-May, and spring sensible heat flux anomalies are close to zero. During summer, the "SIA= SIT1.93–" trajectory exhibits a strong short-wave radiative forcing available to melt sea ice.
455

We further subdivide the net shortwave and longwave radiative surface flux anomalies into their downward and upward components to trace back the net radiative surface flux anomalies to anomalous atmospheric conditions (Figure 7). In the



"SIA= SIT1.93=" trajectory, reduced downward solar radiation and enhanced downward longwave radiation occurs in April-May and May-June (Figure 7(a,c)). The signal in the longwave radiative fluxes are associated with enhanced atmospheric water vapour and cloudiness (Figure 7(e)). In the "SIA= SIT1.93—" trajectory, instead, enhanced downward radiative flux anomalies associated with clouds and water vapour primarily occur in April-May (Figure 7(b,d,f)). In summer, a reduction in clouds occurs and the shortwave radiative fluxes in combination with the sea ice-albedo feedback become the dominant driver of sea ice reduction in both experiments.

5 Discussion and conclusions

We exploit seven initialized ensemble simulations to study the statistical properties of extreme negative summer and late summer pan-Arctic sea ice area anomalies as a function of seven different initial winter states. Likewise, we investigate physical processes in two trajectories leading to extreme late summer sea ice lows with larger amplitudes than the one observed in 2012. In order to circumvent the poor sampling of rare events in numerical simulations, we apply a rare event algorithm to improve the sampling efficiency of trajectories leading to extremely low pan-Arctic sea ice area on average over the melting season and during the annual sea ice minimum. The simulations with the rare event algorithm produce several hundreds of times more extremes than conventional control ensemble simulations for the same computational cost, and allow to generate extreme sea ice lows with probabilities two to three orders of magnitude smaller compared to direct sampling.

The approach used in this study is complementary to the rare event algorithm study of Sauer et al. (2024). In the latter, ensemble simulations are initialized with independent initial conditions sampled from an entire 3000-year control run and the statistics computed with the rare event algorithm corresponds to unconditional probability distributions. Such an approach allows to improve the sampling efficiency of low sea ice states both related to multi-annual variability in the sea ice-ocean system (referred to as "preconditioning" in Sauer et al. (2024)) and driven by the dynamics occurring on intra-seasonal time scales. The single-initial condition approach used in this study, instead, corresponds to a seasonal climate prediction set-up giving access to the probability to observe an extreme late summer sea ice low as a function of a given initial state. This approach also enables a targeted study of intra-seasonal drivers of anomalously strong sea ice reduction during the melting season. Within each ensemble simulation, a contribution of multi-annual sea ice-ocean preconditioning to the generation of low sea ice states compared to the control ensemble mean is by definition excluded as each trajectory starts from the same sea ice-ocean state.

The statistics obtained from the seven different experiments indicates a strong impact of the late winter sea ice initial condition on the probability and amplitudes of extremely negative summer pan-Arctic sea ice area anomalies computed relative to a 3000-year control run baseline climatology. For a fixed probability level, amplitudes of the most extreme February-September and August-September mean sea ice area anomalies span a range of about five and four and a half control run standard deviations over the seven experiments (Figure 3 and table 2). While winter preconditioning is a necessary condition to generate a sea ice low with an amplitude larger than a certain threshold, the most extreme sea ice lows require both preconditioning and anomalous intra-seasonal dynamics (e.g. anomalies in the atmospheric circulation) favouring enhanced reduction of sea ice area during the melting season (Figure 3 and table 2). The relative importance of preconditioning compared to intra-seasonal

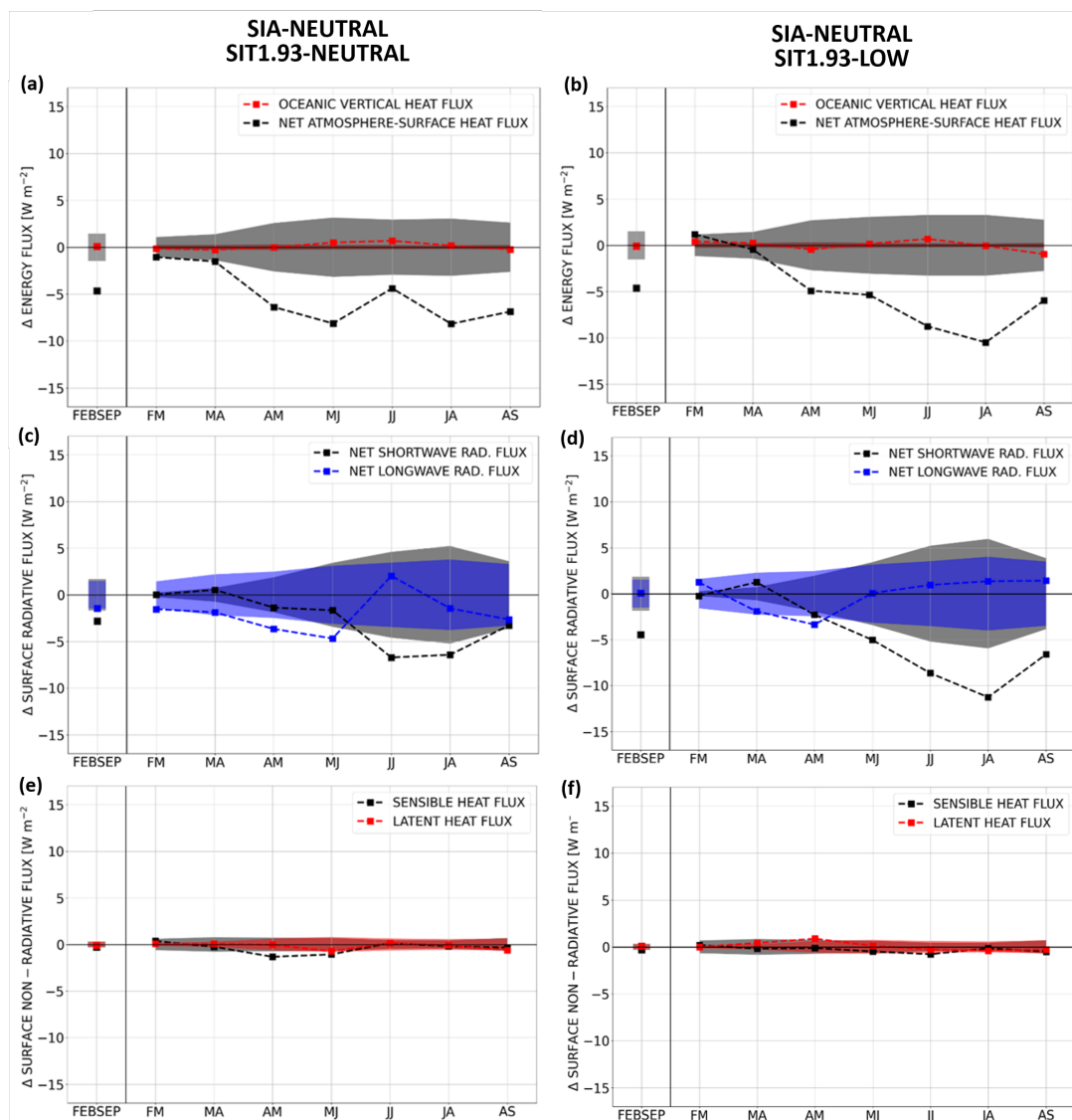


Figure 6. Trajectory with the lowest February-September and August-September mean pan-Arctic sea ice area in the rare event algorithm ensemble simulation starting from a winter initial condition characterized by (a,c,e) neutral sea ice area and neutral SIT1.93 (control run year 1930) and (b,d,f) neutral sea ice area and low SIT1.93 (control run year 1037). Mean energy flux anomalies [W m^{-2}] on average over all ocean grid boxes northern of 70°N . (a-b) (black) Net atmosphere-surface energy flux (sensible + latent + net longwave + net shortwave) and (red) vertical ocean heat flux. (c-d) Net surface (blue) longwave radiative and (black) shortwave radiative flux. (e-f) Surface (red) latent and (black) sensible heat flux anomalies. The sign convention is chosen such that positive anomalies correspond to enhanced upward fluxes. (a-f) Shading indicates anomalies larger in magnitude than the intra-ensemble standard deviation. All anomalies are computed with respect to the climatology of the corresponding control ensembles.

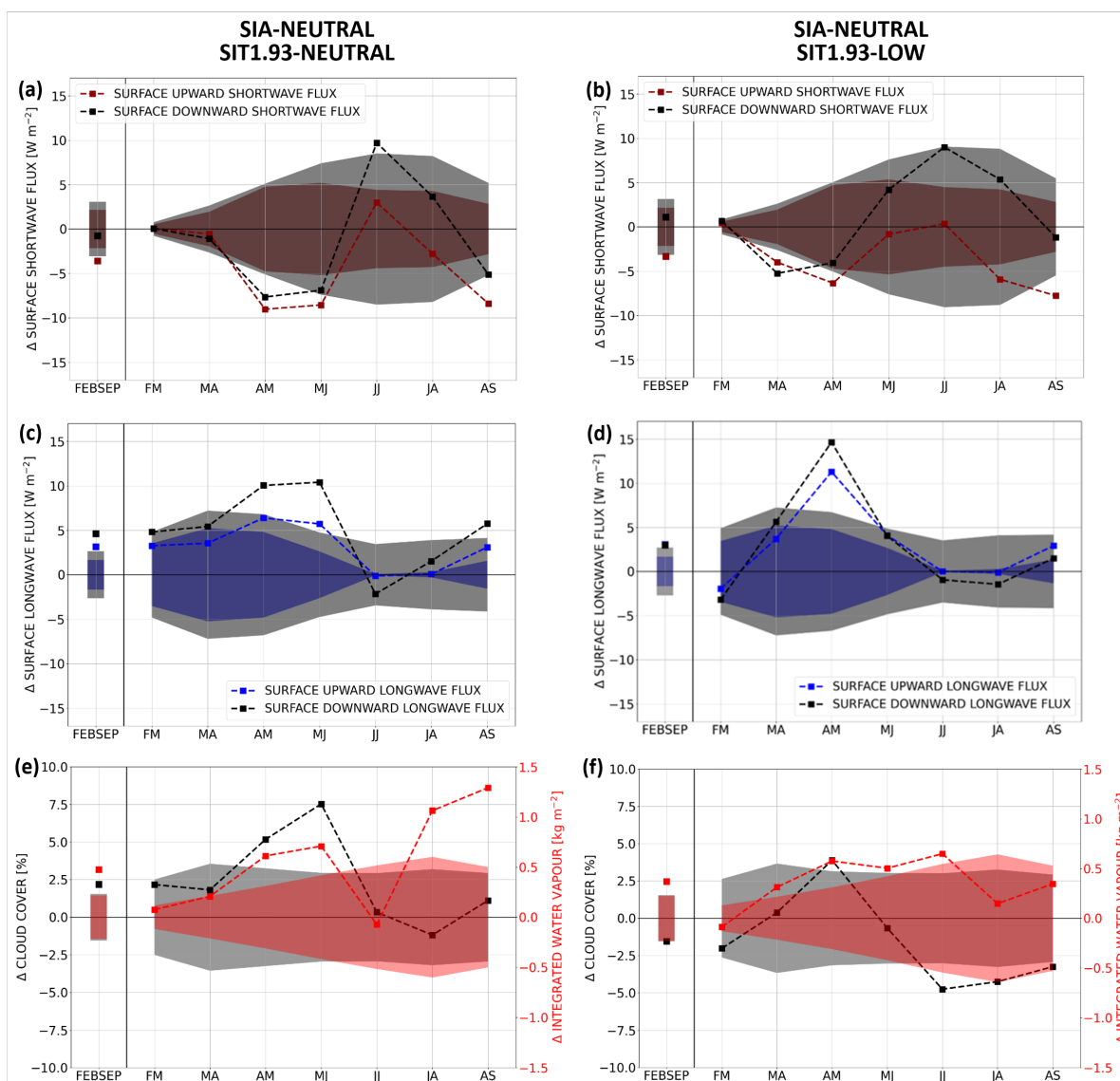


Figure 7. Trajectory with the lowest February-September and August-September mean pan-Arctic sea ice area in the rare event algorithm ensemble simulation starting from a winter initial condition characterized by (a,c,e) neutral sea ice area and neutral SIT1.93 (control run year 1930) and (b,d,f) neutral sea ice area and low SIT1.93 (control run year 1037). Mean anomalies of different quantities spatially averaged over all ocean grid boxes northern of 70°N . (a-b) Surface (darkred) upward and (black) downward shortwave radiative flux anomalies [W m^{-2}]. (c-d) Surface (blue) upward and (black) downward longwave radiative flux anomalies [W m^{-2}]. (a-d) Direction-independent absolute values of the downward and upward fluxes are considered, i.e., a positive (negative) anomaly indicates a radiative flux that is stronger (weaker) in magnitude than the climatology. (e-f) (Black) Total cloud cover [%] and (red) integrated water vapour [kg m^{-2}]. (a-f) Shading indicates anomalies larger in magnitude than the intra-ensemble standard deviation. All anomalies are computed with respect to the climatology of the corresponding control ensembles.



495 dynamics in driving extremely low sea ice area is larger for the February-September than August-September mean sea ice area
(table 2). Thus, at least 50% of the most extremely negative February-September mean sea ice area anomaly in the "SIA–
SIT1.93–" experiment is explainable by the impact of the preconditioning on the control ensemble mean sea ice area (table
2). For August-September, instead, about 36% of the most extremely negative sea ice area anomalies are explainable by the
impact of the preconditioning on the control ensemble mean (table 2).

500 An extremely negative February-September mean pan-Arctic sea ice area anomaly is preconditioned by low January-
February mean states of both the pan-Arctic sea ice area and the cumulative area with sea ice thickness larger than a given
threshold (the precise value used in this study is 1.93 m). In contrast, a source of predictability of an extreme late summer sea
505 ice low is given by the winter sea ice thickness information, but not from the winter sea ice area. Both results are in line with
the memory properties of the sea ice in the Arctic (Blanchard-Wrigglesworth et al., 2011; Chevallier and Salas-Mélia, 2012).
Using a preindustrial simulation with the Centre National de Recherches Météorologiques Coupled Global Climate Model
version 3.3 (CNRM-CM3.3), Chevallier and Salas-Mélia (2012) finds that the cumulative area with sea ice thickness larger
than a threshold between 0.9 and 1.5 m provides a potential source of predictability of the September pan-Arctic sea ice area
510 six months in advance. The authors argue that winter-spring sea ice thickness influences summer sea ice area by modulating the
open-water-formation efficiency during the melting season. The dependency of extremely negative February-September mean
sea ice area anomalies both on the winter SIT1.93 and winter pan-Arctic sea ice area itself can be explained by the fact that late
winter sea ice area anomalies have a non-zero persistence until spring (Blanchard-Wrigglesworth et al., 2011; Chevallier and
Salas-Mélia, 2012). All in all, we emphasize that the precise critical sea ice thickness threshold used to define the cumulative
515 area covered by sea ice thickness larger than a given value and the precise time lag may vary between different models.

We furthermore utilize the rare event algorithm to detect an approximate lower bound of sea ice area values that can be
generated under the constant pre-industrial greenhouse gas forcing used in this study. The lowest August-September mean sea
520 ice area values occurring in this study are in the order of $2 \cdot 10^6$ km². Conditional on starting from a "SIT1.93–" initial winter
state, the estimated probabilities for a sea ice area value equal or below this order of magnitude is 0.001%. Even though this
study may not have detected the initial condition with the most optimal sea ice-ocean properties in favouring low late summer
sea ice area as possible, we conclude that the probability of observing a seasonally sea ice-free Arctic under this set-up is either
close to zero or even zero. We hypothesize that a lower bound of sea ice area values larger than zero is given by sea ice being
525 too thick to be melt away within one season.

Owing to the rare event algorithm, we analyze the physical properties in two individual trajectories leading to extremely
negative August-September mean sea ice area anomalies with conditional probabilities of less than 0.001%. While the precise
530 thermodynamic and dynamical evolution of the atmosphere differs between both trajectories, common mechanisms can be
detected between both trajectories. In both cases, an anomalously strong reduction of the pan-Arctic sea ice area in mid to late
summer is anticipated by the development of negative sea ice thickness anomalies during spring. Apart from a small contribu-
tion of enhanced vertical ocean heat flux anomalies to the reduction of sea ice, the largest amount of net energy accumulation
in the sea ice-ocean system is related to enhanced downward net atmosphere-surface energy fluxes. Within the season, we



535 observe two phases with two different physical properties. During spring, enhanced cloudiness and atmospheric water vapour
results in negative (i.e. downward) net surface longwave radiative flux anomalies, providing enhanced energy to warm or melt
sea ice. This is consistent with the finding of Kapsch et al. (2013, 2019) showing that observed extreme September sea ice
lows have been preceded by enhanced downward longwave radiative fluxes in an anomalously moist and cloudy atmosphere.
During summer, anomalous reduction of sea ice area is favoured by enhanced downward solar radiative flux, the sea ice-albedo
540 feedback and enhanced open water formation efficiency in an anomalously thin sea ice environment.

This study shows how rare event algorithms can be applied to initialized ensembles to study the probability of extreme
states conditional on given initial conditions. This approach could be extremely useful in the context of seasonal to decadal
545 predictions, both in terms of risk quantification, and to inform ensemble initialization strategies by the identification of im-
portant physical drivers for the development of extremes. This would be particularly relevant for applications with complex
numerical models. The present study is based on a relatively low resolution climate model with a purely thermodynamic sea
ice model. A direct dynamic forcing of the atmospheric circulation on the sea ice, e.g., related to synoptic-scale storms or to
the Arctic Oscillation and the Arctic Dipole Anomaly pattern, are therefore not captured by the model. Nevertheless, based on
550 the analysis of two individual trajectories, it illustrates possible thermodynamics states of the atmosphere to generate sea ice
lows larger in magnitude than the one observed in 2012. A similar rare event algorithm study with the EC-Earth model version
3.3.1, including a more complex physics than PlaSim and a dynamic sea ice model is in preparation.



References

- Arakawa, A. and Lamb, V. R.: Computational design of the basic dynamical process of the UCLA general circulation model, *Meth. Comp. Phys.*, 17, 173–265, 1977.
- 555 Årthun, M., Eldevik, T., Smedsrud, L. H., Skagseth, Ø., and Ingvaldsen, R. B.: Quantifying the influence of Atlantic heat on Barents Sea Ice Variability and Retreat, *Journal of Climate*, 25, 4736–4743, <https://doi.org/10.1175/JCLI-D-11-00466.1>, 2012.
- Baldwin, M. P., Stephenson, D. B., Thompson, D. W. J., Dunkerton, T. J., Charlton, A. J., and O’Neill, A.: Stratospheric memory and skill of extended-range weather forecasts, *Science*, 301, 636–640, <https://doi.org/10.1126/science.1087143>, 2003.
- 560 Baxter, I., Ding, Q., Schweiger, A., L’Heureux, M., Baxter, S., Wang, T., Zhang, Q., Harnos, K., Markle, B., Topal, D., et al.: How tropical Pacific Surface Cooling Contributed to Accelerated Sea Ice Melt from 2007 to 2012 as Ice Is Thinned by Anthropogenic Forcing, *Journal of Climate*, 32(24), 8583–8602, <https://doi.org/10.1175/JCLI-D-18-0783.1>, 2019.
- Blanchard-Wrigglesworth, E., Armour, K. C., Bitz, C. M., and DeWeaver, E.: Persistence and inherent predictability of Arctic sea ice in a GCM ensemble and observations, *Journal of Climate*, 24, 231–250, <https://doi.org/10.1175/2010JCLI3775.1>, 2011.
- 565 Bouchet, F., Marston, J. B., and Tangarife, T.: Fluctuations and large deviations of Reynolds stresses in zonal jet dynamics, *Physics of Fluids*, 30, 015 110, <https://doi.org/10.1063/1.4990509>, 2018.
- Chevallier, M. and Salas-Mélia, D.: The role of sea ice thickness distribution in the Arctic sea ice potential predictability: A diagnostic approach with a coupled GCM, *Journal of Climate*, 25, 3025–3038, <https://doi.org/10.1175/JCLI-D-11-00209.1>, 2012.
- Cini, M., Zappa, G., Ragone, F., and Corti, S.: Simulating AMOC tipping driven by internal climate variability with a rare event algorithm, under review, <https://doi.org/10.21203/rs.3.rs-3215995/v1>, 2023.
- 570 Coles, S.: *An Introduction to Statistical Modelling of Extreme Values*, Springer-Verlag, London, 2001.
- Del Moral, P.: *Feynman-kac Formulae Genealogical and Interacting Particle Systems with Applications*, Springer New York, 2004.
- Del Moral, P. and Garnier, J.: Genealogical particle analysis of rare events, *The Annals of Applied Probability*, 15, 2496–2534, <https://doi.org/10.1214/105051605000000566>, 2005.
- 575 Ding, Q., Schweiger, A., L’Heureux, M., Battisti, D. S., P-Chedley, S., Johnson, N. C., Blanchard Wrigglesworth, E., Harnos, K., Zhang, Q., Eastman, R., et al.: Influence of high-latitude atmospheric circulation changes on summertime Arctic sea ice, *Nature Climate Change*, 7, 289–295, <https://doi.org/10.1038/NCLIMATE3241>, 2017.
- Drijfhout, S. S., Maier Reimer, E., and Mikolajewicz, U.: Tracing the conveyor belt in the Hamburg large-scale geostrophic ocean general circulation model, *Journal of Geophysical Research: Oceans*, 101, 22 563–22 575, <https://doi.org/10.1029/96JC02162>, 1996.
- 580 Fetterer, F., Knowles, K., Meier, W. N., Savoie, M., and Windnagel, A. K.: Sea Ice Index, Version 3. National Snow and Ice Data Center, Boulder, CO, digital media, available at <https://doi.org/10.7265/N5K072F8>, 2017.
- Fraedrich, K., Jansen, H., Kirk, E., Luksch, U., and Lunkeit, F.: The Planet Simulator: Towards a user friendly model, *Meteorologische Zeitschrift*, 14, 299–304, <https://doi.org/10.1127/0941-2948/2005/0043>, 2005.
- Francis, J. A. and Wu, B.: Why has no new record-minimum Arctic sea-ice extent occurred since September 2012?, *Environmental Research Letters*, 15, 114 034, <https://doi.org/10.1088/1748-9326/abc047>, 2020.
- 585 Giardina, C., Kurchan, J., Lecomte, V., and Tailleur, J.: Simulating rare events in dynamical processes, *Journal of statistical physics*, 145, 787–811, <https://doi.org/10.1007/s10955-011-0350-4>, 2011.
- Grafke, T. and Vanden-Eijnden, E.: NUMERICAL COMPUTATION OF RARE EVENTS VIA LARGE DEVIATION THEORY, *Chaos*, 29, 063 118, <https://doi.org/10.1063/1.5084025>, 2019.



- 590 Grafke, T., Grauer, R., and Schäfer, T.: The instanton method and its numerical implementation in fluid mechanics, *Journal of Physics A: Mathematical and Theoretical*, 48, 333 001, <https://doi.org/10.1088/1751-8113/48/33/333001>, 2015.
- Gregory, J. M., Stott, P. A., Cresswell, D. J., Rayner, N. A., Gordon, C., and Sexton, D. M. H.: Recent and future changes in Arctic sea ice simulated by the HadCM3 AOGCM, *Geophysical Research Letters*, 29, <https://doi.org/10.1029/2001GL014575>, 2002.
- Guemas, V., Doblas Reyes, F., Germe, A., Chevallier, M., and y Méliá, D. S.: September 2012 Arctic sea ice minimum: Discriminating
595 between sea ice memory, the August 2012 extreme storm, and prevailing warm conditions [in “Explaining Extreme Events of 2012 from a Climate Perspective”], *Bull. Amer. Meteor. Soc.*, 94, S20–S22, 2013.
- Hoven, V. D. I.: Power spectrum of horizontal wind speed in the frequency range from 0.0007 to 900 cycles per hour, *Journal of Atmospheric Sciences*, 14, 160–164, [https://doi.org/10.1175/1520-0469\(1957\)014<0160:PSOHWS>2.0.CO;2](https://doi.org/10.1175/1520-0469(1957)014<0160:PSOHWS>2.0.CO;2), 1957.
- Kahn, H. and Harris, T. E.: Estimation of particle transmission by random sampling, *Natl Bur Stand Appl Math Ser.*, 12, 27–30, 1951.
- 600 Kapsch, M.-L., Graverson, R. G., and Tjernström, M.: Springtime atmospheric energy transport and the control of Arctic summer sea-ice extent, *Nature Climate Change*, 3, 744–748, <https://doi.org/10.1038/NCLIMATE1884>, 2013.
- Kapsch, M.-L., Skific, N., Graverson, R. G., Tjernström, M., and Francis, J. A.: Summers with low Arctic sea ice linked to persistence of spring atmospheric circulation patterns, *Climate Dynamics*, 52, 2497–2512, <https://doi.org/10.1007/s00382-018-4279-z>, 2019.
- Kauker, F., Kaminski, T., Karcher, M., Giering, R., Gerdes, R., and Voßbeck, M.: Adjoint analysis of the 2007 all time Arctic sea-ice
605 minimum, *Geophysical Research Letters*, 36, L03 707, <https://doi.org/10.1029/2008GL036323>, 2009.
- Kirchmeier-Young, M., Zwiers, F. W., and Gillet, N. P.: Attribution of Extreme Events in Arctic Sea Ice Extent, *Journal of Climate*, 30, 553–571, <https://doi.org/10.1175/JCLI-D-16-0412.s1>, 2017.
- Lestang, T., Ragone, F., Bréhier, C.-E., Herbert, C., and Bouchet, F.: Computing return times or return periods with rare event algorithms, *Journal of Statistical Mechanics: Theory and Experiment*, 2018, 043 213, <https://doi.org/10.1088/1742-5468/aab856>, 2018.
- 610 Lestang, T., Bouchet, F., and Lévêque, E.: Numerical study of extreme mechanical force exerted by a turbulent flow on a bluff body by direct and rare-event sampling techniques, *Journal of Fluid Mechanics*, 895, A19, <https://doi.org/10.1017/jfm.2020.293>, 2020.
- Lindsay, R. W., Zhang, J., Schweiger, A. J., and Steele, M. A.: Seasonal predictions of ice extent in the Arctic Ocean, *Journal of Geophysical Research: Oceans*, 113, 1–11, <https://doi.org/10.1029/2007JC004259>, 2008.
- Lindsay, R. W., Zhang, J., Schweiger, A., Steele, M., and Stern, H.: Arctic Sea Ice Retreat in 2007 Follows Thinning Trend, *Journal of
615 Climate*, 22, 165–176, <https://doi.org/10.1175/2008JCLI2521.1>, 2009.
- Maier-Reimer, E., Mikolajewicz, U., and Hasselmann, K.: Mean circulation of the Hamburg LSG OGCM and its sensitivity to the thermohaline surface forcing, *Journal of Physical Oceanography*, 23, 731–757, [https://doi.org/10.1175/1520-0485\(1993\)023<0731:MCOTHL>2.0.CO;2](https://doi.org/10.1175/1520-0485(1993)023<0731:MCOTHL>2.0.CO;2), 1993.
- Meinshausen, M., Vogel, E., Nauels, A., Lorbacher, K., Meinshausen, N., Etheridge, D. M., Fraser, P. J., Montzka, S. A., Rayner, P. J.,
620 Trudinger, C. M., et al.: Historical greenhouse gas concentrations for climate modelling (CMIP6), *Geoscientific Model Development*, 10(5), 2057–2116, <https://doi.org/10.5194/gmd-10-2057-2017>, 2017.
- Notz, D. and Marotzke, J.: Observations reveal external driver for Arctic sea-ice retreat, *Geophysical Research Letters*, 39, 1–6, <https://doi.org/10.1029/2012GL051094>, 2012.
- Notz, D. and SIMIP Community: Arctic sea ice in CMIP6, *Geophysical Research Letters*, 47(10), 1–11,
625 <https://doi.org/10.1029/2019GL086749>, 2020.
- Ogi, M., Rysgaard, S., and Barber, D. G.: Importance of combined winter and summer Arctic Oscillation (AO) on September sea ice extent, *Environmental Research Letters*, 11, 034 019, 2016.



- Ono, J., Tatebe, H., and Komuro, Y.: Mechanisms for and Predictability of a Drastic Reduction in the Arctic Sea Ice: APPOSITE data with Climate Model MIROC, *Journal of Climate*, 32, 1361–1380, <https://doi.org/10.1175/JCLI-D-18-0195.1>, 2019.
- 630 Overland, J. E., Francis, J. A., Hanna, E., and Wang, M.: The recent shift in early summer Arctic atmospheric circulation, *Geophysical Research Letters*, 39, L19 804, <https://doi.org/10.1029/2012GL053268>, 2012.
- Parkinson, C. L. and Comiso, J.: On the 2012 record low Arctic sea ice cover: Combined impact of preconditioning and an August storm, *Geophysical Research Letters*, 40, 1356–1361, <https://doi.org/10.1002/grl.50349>, 2013.
- Plotkin, D. A., Webber, R. J., O’Neill, M. E., Waere, J., and Abbot, D. S.: Maximizing simulated tropical cyclone intensity with action
635 minimizing, *Journal of Advances in Modeling Earth Systems*, 11, 863–891, <https://doi.org/10.1029/2018ms001419>, 2019.
- Ragone, F. and Bouchet, F.: Computation of Extreme Values of Time Averaged Observables in Climate Models with Large Deviation Techniques, *Journal of Statistical Physics*, 179, 1637–1665, <https://doi.org/10.1007/s10955-019-02429-7>, 2020.
- Ragone, F. and Bouchet, F.: Rare event algorithm study of extreme warm summers and heatwaves over Europe, *Geophysical Research Letters*, 48, e2020GL091 197, <https://doi.org/10.1029/2020GL091197>, 2021.
- 640 Ragone, F., Wouters, J., and Bouchet, F.: Computation of extreme heat waves in climate models using a large deviation algorithm, *Proceedings of the National Academy of Sciences*, 115, 24–29, <https://doi.org/10.1073/pnas.1712645115>, 2018.
- Rigor, I. G., Wallace, J. M., and Colony, R. L.: Response of Sea Ice to the Arctic Oscillation, *Journal of Climate*, 15, 2648–2663, [https://doi.org/10.1175/1520-0442\(2002\)015<2648:ROSITT>2.0.CO;2](https://doi.org/10.1175/1520-0442(2002)015<2648:ROSITT>2.0.CO;2), 2002.
- Sauer, J., Demayer, J., Zappa, G., Massonnet, F., and Ragone, F.: Extremes of summer Arctic sea ice reduction investigated with a rare event
645 algorithm, *Climate Dynamics*, pp. 1–19, <https://doi.org/10.1007/s00382-024-07160-y>, 2024.
- Schweiger, A. J., Zhang, J., Lindsay, R. W., and Steele, M.: Did unusually sunny skies help drive the record sea ice minimum of 2007?, *Geophysical Research Letters*, 35, <https://doi.org/10.1029/2008GL033463>, 2008.
- Semtner, A. J.: A Model for the Thermodynamic Growth of Sea Ice in Numerical Investigations of Climate, *Journal of Physical Oceanography*, 6, 379–389, 1976.
- 650 Serreze, M. C. and Barry, R. G.: *The Arctic Climate System*, Cambridge Atmospheric and Space Science Series, J. T. Houghton, M. J. Rycroft and A. J. Dessler (editors.), Cambridge University Press, 2014.
- Stroeve, J. and Notz, D.: Changing state of Arctic sea ice across all seasons, *Environmental Research Letters*, 13, 1–23, <https://doi.org/10.1088/1748-9326/aade56>, 2018.
- Tietsche, S., Notz, D., Jungclaus, J. H., and Marotzke, J.: Recovery mechanisms of Arctic summer sea ice, *Geophysical Research Letters*,
655 38(2), <https://doi.org/10.1029/2010GL045698>, 2011.
- Wang, J., Zhang, J., Watanabe, E., Ikeda, M., Mizobata, K., Walsh, J. E., Bai, X., and Wu, B.: Is the Dipole Anomaly a major driver to record lows in Arctic summer sea ice extent?, *Geophysical Research Letters*, 36, L05 706, <https://doi.org/10.1029/2008GL036706>, 2009.
- Webber, R. J., Plotkin, D. A., O’Neill, M. E., Abbot, D. S., and Waere, J.: Practical rare event smapling for extreme mesoscale weather, *Chaos*, 29, 053 109, <https://doi.org/10.1063/1.5081461>, 2019.
- 660 Woodgate, R. A., Weingartner, T., and Lindsay, R.: The 2007 Bering Strait oceanic heat flux and anomalous Arctic sea-ice retreat, *Geophysical Research Letters*, 37, L01 602, <https://doi.org/10.1029/2009GL041621>, 2010.
- Wouters, J., Schiemann, R. K. H., and Shaffrey, L. C.: Rare event simulation of extreme European winter rainfall in an intermediate complexity climate model, *Journal of Advances in Modeling Earth Systems*, 15, e2022MS003 537, <https://doi.org/10.1029/2022MS003537>, 2023.

<https://doi.org/10.5194/egusphere-2024-3082>

Preprint. Discussion started: 10 October 2024

© Author(s) 2024. CC BY 4.0 License.



665 Zhang, J., Lindsay, R., Steele, M., and Schweiger, A.: What drove the dramatic retreat of arctic sea ice during summer 2007?, *Geophysical Research Letters*, 35, L11 505, <https://doi.org/10.1029/2008GL034005>, 2008.

Zhang, J., Lindsay, R., Schweiger, A., and Steele, M.: The impact of an intense summer cyclone on 2012 Arctic sea ice retreat, *Geophysical Research Letters*, 40, 720–726, <https://doi.org/10.1002/grl.50190>, 2013.



Appendix A

670 *Code and data availability.* The code and data availability will be indicated after acceptance of the article.

Author contributions. All authors contributed to the study conception and design. Model simulations, data collection and analyses were performed by the first author Jerome Sauer. The first draft of the manuscript was written by the first author Jerome Sauer and all authors commented on previous versions of the manuscript. All authors read and approved the final manuscript.

Competing interests. The authors declare that they have no conflict of interest.

675 *Special issue statement.* The manuscript has been produced in the context of a cross-journal special issue, lead by the European Geosciences Union's (EGU's) Earth System Dynamics. The special issue also includes the journals Geoscientific Model Development (GMD) and Nonlinear Processes in Geophysics (NPG). The topic of the special issue is "Theoretical and computational aspects of ensemble design, implementation and interpretation in climate science".

680 *Funding.* This publication is supported by the FSR Seedfund program and by the French Community of Belgium as part of a FRIA (Fund for research training in industry and agriculture) grant.

Acknowledgements. Computational resources have been provided by the supercomputing facilities of the Université catholique de Louvain (CISM/UCL) and the Consortium des Équipements de Calcul Intensif en Fédération Wallonie Bruxelles (CÉCI) funded by the Fond de la
685 Recherche Scientifique de Belgique (F.R.S.-FNRS) under convention 2.5020.11 and by the Walloon Region. This project is supported by the Belgian Science Policy (BELSPO) project RESIST (CONTRAT N° RT/23/RESIST). This project is also supported by the European Union (ERC, ArcticWATCH, 101040858). Views and opinions expressed are however those of the author(s) only and do not necessarily reflect those of the European Union or the European Research Council Executive Agency. Neither the European Union nor the granting authority can be held responsible for them. François Massonnet is a F.R.S.-FNRS Research Associate. GZ has been supported by the "Programma di
690 Ricerca in Artico" (PRA; project no. PRA2019-0011, SENTINEL).